Transmission near-field scanning microscope for infrared chemical imaging

Bogdan Dragnea, Jan Preusser,[a] Wolfgang Schade,[a] and Stephen R. Leone[b]
Departments of Chemistry and Physics, JILA, National Institute of Standards and Technology and University of Colorado, Boulder, Colorado 80309-0440

William D. Hinsberg
IBM Almaden Research Center, 650 Harry Road, San Jose, California 95120-6099

(Received 25 March 1999; accepted for publication 28 May 1999)

We report transmission infrared near-field scanning microscopy (IR-NSOM) imaging of chemically amplified photoresist polymers patterned by ultraviolet exposure. Chemical specificity was attained using infrared wavelengths tuned to the 3 μm OH stretch absorption band of the polymer, a band sensitive to the chemical changes characteristic of the lithographic photochemical process of this material. Contrast mechanisms are discussed together with the IR-NSOM specifics, such as the fabrication of an infrared near-field probe with high throughput, which lead to an attainable resolution of $\lambda/10$ and a transmission sensitivity of 1%. © *1999 American Institute of Physics.* [S0021-8979(99)05917-4]

INTRODUCTION

Infrared near-field scanning optical microscopy (IR-NSOM) combines the potential for high spatial resolution with vibrational spectroscopy capabilities. Despite these two appealing features, there are few reports of IR and microwave near-field microscopy[1–5] compared to the visible counterpart, and no subwavelength resolution images exhibiting chemical contrast have been obtained, although significant progress has been made.[6,7] The extension of visible NSOM techniques to the IR has been hindered to date by several obstacles.

First, fiber-optic-based NSOMs exhibit limitations caused by the transparency range of fiber materials. Optical, mechanical, and thermal requirements, as well as the cost, when considered together, indicate that no infrared fiber material fulfills all of these as well as fused silica does for the visible range.[8] Second, the cutoff diameter of a circular waveguide is proportional to the wavelength. It follows that in the case of a conical tip the distance that the light has to travel to the aperture while in the evanescent regime will be proportional to the wavelength.[9] The attenuation of the light is exponential in this zone; thus, we expect the following transmittance relation, $T_{IR}=(T_{VIS})^5$ (where 5 approximates the ratio $\lambda_{IR}/\lambda_{VIS}$) between the transmittance of the fiber in the IR, T_{IR}, and in the visible, T_{VIS} (assuming the same taper and optical properties). Tapered fiber transmittances range from 10^{-4} to 10^{-5} in the visible depending on method and aperture diameter (Ref. 10, and references therein). Therefore, in the IR one expects transmittances of only 10^{-9}–10^{-12}. Third, while a typical visible NSOM uses photomultipliers or avalanche photodiodes for detection with detectivities of $\sim 10^{16}\,\mathrm{Hz}^{1/2}\,\mathrm{cm\,W}^{-1}$, liquid-nitrogen-cooled photoconductive detectors used around 3 μm do not achieve better than a few a $10^{11}\,\mathrm{Hz}^{1/2}\,\mathrm{cm\,W}^{-1}$. Finally, cross sections associated with vibrational bands are generally smaller than those associated with electronic transitions and one expects accordingly less contrast from a ''vibrational'' band-specific image.

These difficulties have contributed to the slower development of IR-NSOM. The most popular NSOM configuration in the visible—the transmission-mode NSOM—is totally absent in the IR. The most representative attempts in the IR region used an apertureless, metallic tip[2,5] as a scatterer. The use of an apertureless tip eliminates fiber-related problems. However, when not used in a total reflection or fluorescence arrangement, a scattering apertureless IR-NSOM of the type used in Refs. 2 and 5 is prone to cross talk between topographic and optically induced signals, since the illuminated spot radius is much larger than the probe apex radius. Separation of these contributions is possible but it increases the complexity of the experimental setup.[11,12]

In this article we describe an IR-NSOM dedicated to the study of chemical changes occurring upon photoimaging of polymer photoresist thin films of interest in microlithography. Photoresist patterning is one of the few processes in integrated-circuit fabrication that is run without a closed feedback loop. Latent image metrology provides the means to study the evolution of the resist profile at different steps of the pattern formation: after exposure, postexposure bake, and development.[13] When measured by IR-NSOM, the results could provide information on topography as well as on optical properties, namely, on those related to chemical bond formation.

EXPERIMENT

The samples are films of poly(*t*-butylmethacrylate) (PTBMA) containing 5 wt% of the photoacid generator

[a]Present address: TU Clausthal, Physikalisches Institut, Leibnizstrasse 4, 38678 Clausthal–Zellerfeld, Germany.
[b]Author to whom correspondence should be addressed: Quantum Physics Division, National Institute of Standards and Technology; electronic mail: srl@jila.colorado.edu

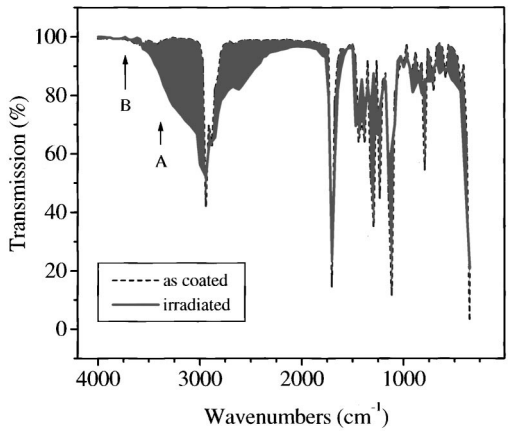

FIG. 1. PTBMA IR absorption spectra for exposed and as-coated films. The arrows point to the wavelengths used for the IR image in Fig. 5.

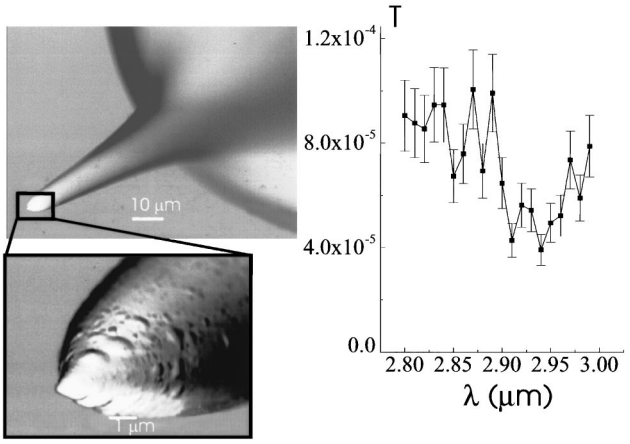

FIG. 2. Left: SEM picture of a pulled fluoride tip by the two-step-controlled velocity method. One can notice in the closeup the second abrupt taper of the fiber. Right: tip transmissivity vs. wavelength. Fluctuations are reproducible from one wavelength scan to another and may be due to the coupling efficiency of the transmitted light by the multimode tapered fiber, at different wavelengths.

triphenylsulfonium hexafluoroantimonate (TPS-SbF_6) on sapphire wafers. The samples were patterned by contacting a chrome/quartz mask with the wafer and exposing, through the mask, with a predetermined dose of light at wavelength 250 nm. This causes the photoacid generator to form hexafluoroantimonic acid, a very strong acid. Heating at 130 °C for 1–5 min activates the acid-catalyzed thermal chemistry. The most prominent changes in the IR spectra are a broadening in the carbonyl region near 1750 cm^{-1} due to conversion of the ester to a hydrogen-bonded carboxylic acid, and the appearance of broad hydroxyl absorption between 3000 and 3600 cm^{-1}, Fig. 1. The patterns are 500 nm line/500 nm space and 1000 nm line/1000 nm space on films of thicknesses 250 and 1000 nm, respectively.

The near-field microscope is a conventional setup: a transmission NSOM with an aperture probe,[9] however, with an infrared transparent fiber. The IR radiation (4 mW, chopped at 100 Hz), tunable between 3550 and 3125 cm^{-1}, is provided by a color-center laser pumped by a Kr^+-ion laser, chopped at 90 Hz. We are able, therefore, to probe modifications occurring within the hydroxyl absorption band. The tip is obtained by fiber pulling using a commercial micropipette puller combined with a rf-powered CO_2 laser.[14] Several fiber materials were tested: fluoride, chalcogenide, sapphire, and low-OH silica fibers. We found that at 3 μm, fluoride fibers (53%ZrF_4–20%BaF_2–4%LaF_3–3%AlF_3–20%NaF) of 0.2 mm diameter represented the best compromise, taking into account optical, mechanical, and thermal properties and cost.

As mentioned, the progression from visible to IR-NSOM is not straightforward, a necessary step being the improvement of throughput of the tapered fiber probe. In order to do this we estimated first the dynamics of the fiber pulling. This was accomplished by coupling the light from a He–Ne laser into the fiber and measuring the output on a photodiode with an oscilloscope during the pulling. The CO_2 laser power density was 10 W/cm^2, and the cross section of the beam in the fiber plane ~1 mm^2. The result of this analysis shows that by using conventional pulling methods,[14] the pulling takes approximately 100 ms while the cutoff diameter for guided propagation occurs at ~5 ms before the final separation of the fiber. The pulling parameters (heating power, pulling speed, time) can be controlled dynamically up to 1 ms. Knowing that fast pulling velocities lead to long tapers while slow pulling velocities lead to blunt tips and short tapers, a two-step pulling technique was adopted in which we begin by a slow pull resulting in a taper larger than the wavelength of light, and just before the end, we elongate the remaining molten material in a second abrupt taper ending in a sharp tip.

A typical result of this pulling method is presented in the scanning electron microscope (SEM) images of Fig. 2(a). After coating with 120 nm of Al, a 200–300 nm diam aperture is obtained at the tip. Figure 2(b) shows the tapered fiber transmittance (measured relatively to a cleaved end fiber) at wavelengths around 2.9 μm. The 10^{-4} transmittance represents a factor of 10^5 improvement compared to what one would expect from a conventionally pulled tip of the same aperture.

The detection efficiency of the IR light has been improved by integrating the detector (300 K, PbS cell, 24 mm^2) directly into the sample holder, very close to the tip/sample interaction region (2 mm); in far field, the measured divergence angle of the emerging IR light from the tip is ~80°. With a time constant of the lock-in amplifier of 1 ms, the signal-to-noise ratio on the PbS detector is typically between 100 and 200. This limits the sensitivity to transmittance variations of ~1%.

RESULTS

The shear-force method was employed for tip/sample distance control. Two 6×6 μm and 3×3 μm images of surface topography of the polymer films are shown in Fig. 3. A pattern of lines is clearly visible, the result of thinning of the exposed regions of the film due to the evolution of isobutylene upon acid-catalyzed thermolysis. We found a maximum height variation of 210 nm (for a light exposure of 43 mJ/cm^2, and a film thickness of 1000 nm) by confocal inter-

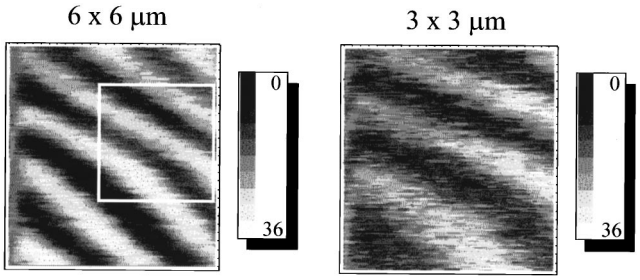

FIG. 3. Topographic (constant shear-force) images acquired from a PTBMA-exposed film (250 nm thick) on sapphire. The lines (dark) and the spaces (light) on the mask used for irradiation are 1 μm wide. The right panel contains a closeup of the left panel (indicated by the square).

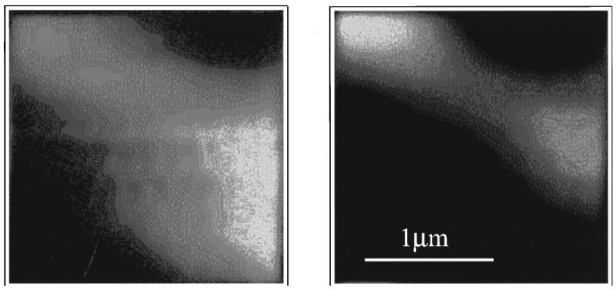

FIG. 5. IR NSOM images for 1-μm-thick films, 1 μm lines, taken at two different wavelengths: (left) 3420 cm^{-1} (within the absorption band of the irradiated polymer, but out of it for nonirradiated zones), and (right) 3640 cm^{-1} (away from any absorption features). The irradiated lines are the diagonal lighter regions.

ferometric microscopy at 638 nm. However, the maximum height variation measured by NSOM on the different sample in Fig. 3 was ~36 nm. The calibration has been made taking into account the amplifier gain and the piezoelectric constant for the vertical actuator. The sample imaged by NSOM had imperfect mask contact during the UV exposure, while much better contact was achieved on the samples investigated by confocal interferometric microscopy. Some of the UV light probably leaked under the mask in the case of the NSOM samples and this can explain why there is less height contrast. The scanner tube used in our setup was not linearized, so some bending and variation in feature dimensions can occur. However, the bending seen in the 3×3 μm closeup view in Fig. 3 cannot be attributed to such an artifact. The bending can be due to the same possible thickness nonuniformity that prevented the contact between the mask and the film during irradiation. Long-range scanning confocal microscopy images confirmed the local bending observed in Fig. 3. However, the cause appears to be surface scratches and swellings that deform the film over relatively wide areas.

An IR-NSOM image taken simultaneously with the topographic one is presented in Fig. 4. The film thickness is 250 nm while the features on the sample are 500 nm lines separated by 500 nm spaces. The IR wavelength is 2.94 μm (3400 cm^{-1}), well within the photochemically broadened OH absorption band (Fig. 1). Analysis of the two figures shows

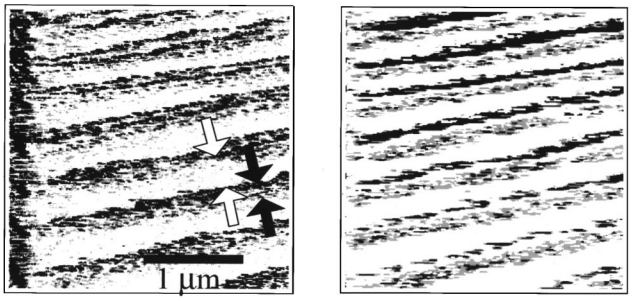

FIG. 4. IR transmission (left) and topographic (right) pictures of a 250-nm-thick exposed film (21 mJ/cm^2) with 500 nm line/space features. It roughly represents the present limit of sensitivity (1%) and resolution (~300 nm) of our microscope. Exposed areas are dark on the optical and topographic images, corresponding to less optical transmission and the shrinkage regions of the film. Exposed lines appear narrower in the topographic image (black arrows) than the unexposed lines (white arrows) due to the ''tip shadowing'' effect.

that the irradiated lines (lower NSOM transmission signal) correspond to deeper lines in the topographic image (darker regions), indicating shrinkage of the irradiated regions. The best optical resolution obtained from Fig. 4 is ~300 nm (λ/10). Figure 4 also displays unequal line dimensions, especially in the topographic image, the narrow ones being deeper than the wide ones. Narrowing of the deeper features is a common effect in shear-force microscopes, known as the tip ''shadowing'' effect; due to the finite-tip radius, the tip cannot accurately follow the deeper features. Our aperture is ~200 nm and the aluminum coating 120 nm, for a total tip diameter of 440 nm, close to the feature dimensions in Fig. 4. The tip dithering amplitude of ~50 nm will further increase the tip shadowing. If one compares the topographic images from Fig. 3 (1 μm lines) and Fig. 4 (0.5 μm lines) one can notice that the narrowing effect of the deeper lines increases with decreasing pattern spacing, which is consistent with the ''tip shadowing'' explanation. Given the signal-to-noise ratio of a typical scan, a 1% transmission change can be detected.

Significant differences appear when using different IR wavelengths, as shown in Fig. 5 (1 μm lines, 1 μm film thickness). For the left-panel image we used 3420 cm^{-1} (point A on Fig. 1), within the absorption tail of the O–H band, but only for the regions irradiated by the 250 nm light. The right-panel image was acquired using radiation at 3640 cm^{-1}, completely away from both absorptions for exposed and unexposed areas (point B, Fig. 1). Both images are taken in constant height mode in order to reduce the possibility of topographic artifacts in the optical image.[9] The dark regions correspond in this case to less absorption.

Two facts are worth noting concerning the thicker films of Fig. 5. First, the UV-exposed line dimension is quantitatively larger when the resonant wavelength is used (3420 cm^{-1}). Second, one gets an image of the line even when the OH absorption is near zero for both the irradiated and nonirradiated zones.

The explanation of these features requires consideration of the contrast mechanisms in relation with the resolution at resonant wavelengths, the achievable chemical (vibrational) contrast and the overall contrast. We will concentrate first on the contrast at nonresonant wavelengths (right panel in Fig. 5). The experimental contrast of this image is 10% while the

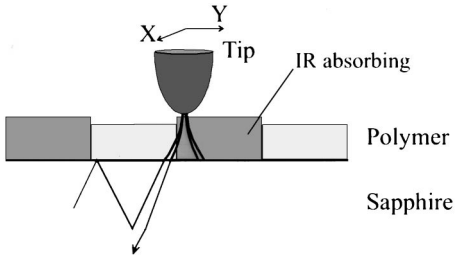

FIG. 6. Spreading of the angular distribution of the probe light in absorptive and refractive contrast mechanisms. In the case of a thick film, the envelope of light includes, at the same time, exposed and unexposed zones of the polymer. This limits the resolution of the *absorptive contrast* mechanism. The cone angle effect is illustrated by the total internal reflection at the sapphire–air interface.

contrast at 3420 cm^{-1} (left panel in Fig. 5) is 15%. It follows that in the overall contrast there is a major nonresonant component. There is no absorption at 3640 cm^{-1}, therefore, the contrast must be refractive in origin. There are two possibilities: (1) the real part of the index of refraction changes when moving from an UV-exposed region to a nonexposed region. (2) The thickness of the exposed film is different from that of the nonexposed film and multiple reflections occur. Both situations lead to different reflection coefficients for the exposed and unexposed films, and therefore, different external transmittances.

The reported refractive index for PTBMA at the sodium *D* line (589 nm) is $n=1.464$,[15] and the poly(acrylic acid), a close analog of poly(methylmethacrylate) (the deprotected form of PTBMA) has $n=1.5$. At this wavelength *and for a collimated beam*, the far-field variation of transmittance, due to the index of refraction modification subsequent to UV exposure, should be ~0.5%.

The film thickness variation causes an external transmission variation only if multiple reflections occur. In this case, and considering the above variation in the real part of the index of refraction and *a collimated beam*, one expects only a 4% contrast in the visible region. It should, therefore, be possible to obtain NSOM images of patterned photoresist films at visible wavelengths, and this experiment has also been realized in our laboratory. However, the observed contrast is as high as 18% (at 675 nm, Kr-ion laser) even though there is no observable absorption. The contrast using visible light (675 nm, 18%) is higher than the maximum contrast with IR light (~2900 nm, 10%–15%), where there is an absorption. Therefore, calculations of the contrast based on collimated beams and far-field refractive effects give results significantly smaller than the experimental ones. It follows that the source of contrast must be related to the actual geometrical shape of the beam, collimated in the near field and divergent in the far field.[16]

The fact that the beam is collimated at the exit of the tip for distances comparable to the aperture diameter, while it has a divergence of ~80° in the far field, indicates that some of the light rays are totally reflected by the sapphire substrate at the air interface, Fig. 6.[17] The refraction angles are different at the polymer/sapphire interface for exposed and unexposed areas. Therefore, a different amount of light will be totally reflected at the sapphire/air surface as the tip is located above exposed or unexposed regions of the polymer. The difference in the maximum angle of transmitted light in these two cases gives rise to a contrast of refractive origin, called here the cone angle effect. Using the difference in the real part of the indices of refraction for the exposed and unexposed polymers, in the visible, we estimate this contrast at approximately 11%, the same order of magnitude as the experimental one. These estimates show that, in our case, this is the main mechanism for the overall contrast, when no absorption is present. The contrast magnitude is proportional, in this case, to the numerical aperture of the collection optics.

To investigate the contrast mechanisms further, we performed confocal microscopy imaging, with 632 nm laser light, of similarly prepared samples, but with 16 μm features. The same contrast as found in the NSOM images at 675 nm was observed. However, classical microscopy using collimated light from a lamp yielded a much lower contrast (<5%). From this comparison of three different techniques, NSOM, confocal, and classical, we can infer two conclusions. First, a possible enhancement of the contrast of the visible NSOM images by a topographic artifact can be ruled out since the same contrast is obtained with the confocal microscope—a far-field technique. Second, one obtains more than 15% contrast only when using focused beams with a different divergence in the near and far fields. This suggests that the refractive cone angle effect accounts, indeed, for most of the contrast.

Let us consider now the chemical effect observable as a difference of ~5% in the contrast of the images of Fig. 5. In the IR, in addition to the mechanism related to the real part of the index of refraction, there is also contrast given by the difference in the absorption coefficient between exposed and unexposed areas. Again, the IR light emitted by the NSOM tip has a certain angular distribution varying with the distance from the tip. It follows that thicker films, together with the large cone angle of IR light emitted from the NSOM tip, will spatially broaden the absorbing region, Fig. 6.

The result of far-field integration of the transmitted IR light over the angular range of emission is presented in Fig. 7. The observable modulation is shown only for the effect of the absorption coefficient (at the resonant wavelength) as the tip scans the surface. An ideal tip of aperture much less than the surface features has been considered. One can infer from these simple calculations that the resolution is limited in the case of thick polymer films by the far-field effect of angular averaging during collection. One can avoid this by decreasing the numerical aperture of the collection optics at the expense of sensitivity. Also, the calculated contrast for 1-μm-thick films, of about 4%, agrees well with the contrast difference between the resonant and nonresonant wavelength images (~5%). The difference in film thickness does not contribute significantly at IR wavelengths since this is very small compared to the wavelength.

In summary, the image obtained at 3420 cm^{-1} (Fig. 5, 15% contrast) carries information on both the real and imaginary parts of the complex index of refraction, whereas the image at 3640 cm^{-1} (10% contrast) is determined only by the real index modifications. The refractive index mechanism

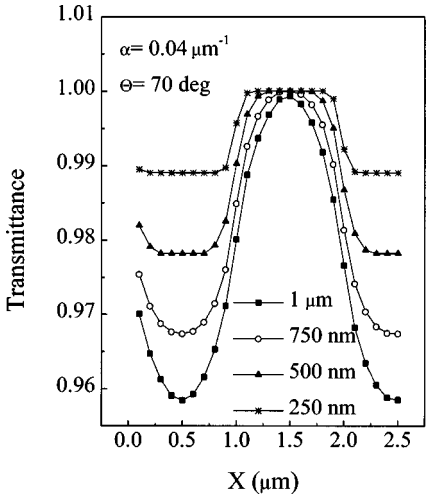

FIG. 7. Calculated IR transmittance of the patterned film (1μm lines spacing) for different film thicknesses. Only the absorption mechanism was considered. The increase in contrast can be achieved at the expense of resolution for thicker films. For 1-μm-thick film and 1 μm lines spacing, the detection spatial bandwidth equals approximately the period of the pattern.

is much less sensitive to absorption features in the IR since it is mainly determined (according to Kramers–Krönig relationships) by the very intense absorption band in the UV (the calculated effect on the external transmittance due to the change in index with the IR wavelength is less than 0.1%). The only mechanism that makes a measurable difference between these two IR wavelengths is the imaginary part of the complex index of refraction (pure absorption). Knowing that the broadening of the infrared OH absorption band is related to extensive bond modifications occurring during the photochemistry, we characterize the qualitative differences between the two images as due to the infrared chemical sensitivity of the pure absorption contrast mechanism. For 1-μm-thick polymers this effect accounts for an ~5% variation in transmission (obtained as the difference in contrast for the two wavelengths). Thus, the result represents a promising approach for chemical-species-specific NSOM probing.

CONCLUSION

In conclusion, IR-NSOM with chemical sensitivity has been realized using a conventional transmission setup with high transmittance fiber tips, pulled by a two-step technique and improved detection. In the case of patterned PTBMA films, the images are the result of modifications to the real and imaginary parts of the index of refraction. The real part carries information about modifications occurring at wavelengths within the strongest absorption band of the material: in the case of PTBMA, this is in the UV. This nonresonant contrast mechanism can be useful to map the interaction between the UV radiation and material. The chemical sensitivity is determined mainly by modifications to the imaginary part of the index of refraction (absorption), and it has a smaller but clear contribution. This mechanism could be used for experimental determination of photoacid diffusion in photoresists,[18,19] provided the resolution of the NSOM can be decreased to ~10 nm with good sensitivity.

ACKNOWLEDGMENTS

The authors thank Frances Houle for many important discussions. The authors also gratefully acknowledge financial support by the National Institute of Standards and Technology and by the National Science Foundation.

[1] A. Piednoir, C. Licoppe, and F. Creuzet, Opt. Commun. **129**, 414 (1996).
[2] A. Larech, R. Bachelot, P. Gleyzes, and A. C. Boccarra, Appl. Phys. Lett. **71**, 575 (1997).
[3] B. Knoll, F. Keilmann, A. Kramer, and R. Guckenberger, Appl. Phys. Lett. **70**, 2667 (1997).
[4] F. Keilmann, in *Optics at the Nanometer Scale*, edited by M. Nieto-Vesperinas and N. Garcia, ASI NATO series (Kluwer Academic, Boston, 1996), Vol. 319, pp. 235–245.
[5] B. Knoll and F. Keilmann, Appl. Phys. A: Mater. Sci. Process. **66A**, 477 (1998).
[6] D. A. Smith, S. Webster, M. Ayad, S. D. Evans, D. Fogherty, and D. Batchelder, Ultramicroscopy **61**, 247 (1995).
[7] C. E. Jordan, S. J. Stranik, R. R. Cavanagh, and L. J. Richter, Surf. Sci. (to be published).
[8] J. S. Sanghera and I. D. Aggarwal, *Infrared Fiber Optics* (CRC, Boca Raton, FL, 1998).
[9] E. Betzig and J. K. Trautmann, Science **257**, 189 (1992).
[10] T. Yatsui, M. Kourogi, and M. Ohtsu, Appl. Phys. Lett. **73**, 2090 (1998).
[11] F. Zenhausern, M. P. O'Boyle, and H. K. Wicramasinghe, Appl. Phys. Lett. **65**, 1623 (1994).
[12] K. Fukuzawa and Y. Tanaka, Appl. Phys. Lett. **71**, 169 (1997).
[13] J. A. Liddle, T. A. Fernandez, R. Cirelli, M. M. Mkrtchyan, A. E. Novembre, M. L. Peabody, and G. P. Watson, J. Vac. Sci. Technol. B **15**, 3163 (1997).
[14] G. A. Valaskovic, M. Holton, and G. H. Morrison, Appl. Opt. **34**, 1215 (1995).
[15] D. Van Krevelin, *Properties of Polymers* (Elsevier, New York, 1976), p. 219.
[16] J. P. Fillard, *Near Field Optics and Nanoscopy* (World Scientific, Singapore, 1996), p. 53.
[17] E. B. McDaniel and J. W. P. Hsu, J. Appl. Phys. **81**, 2488 (1997).
[18] T. Itani, H. Yoshino, S. Hashimoto, M. Yamana, N. Samoto, and K. Kasama, J. Vac. Sci. Technol. B **14**, 4226 (1996).
[19] P. M. Dentinger, B. Lu, and J. W. Taylor, J. Vac. Sci. Technol. B **16**, 3767 (1998).